Article

Promoting Fast Ion Conduction in Li-Argyrodite through Lithium Sublattice Engineering

Po-Hsiu Chien, Bin Ouyang,* Xuyong Feng,* Lei Dong, David Mitlin, Jagjit Nanda, and Jue Liu*

ACCESS | Metrics & More | Article Recommendations | SI Supporting Information

ABSTRACT: Fundamental understanding of ionic transport plays a pivotal role in designing and optimizing fast ionic conductors. Here, through a systematic neutron scattering and theoretical investigation, we discovered new insights about how anion sublattice affects Li^+ distribution and transport in Li-argyrodite. We found that the promotion of Li^+ conductivities is strongly correlated with a previously overlooked Li^+ interstitial site (16e), which is critical for realizing intercage Li^+ migration. More isotropic Li^+ migration pathways with higher Li^+ occupancies on the interstitial 16e site are found to be the underlying reason for the much higher Li^+ conductivity in Li_6PS_5Cl relative to the Br- and I-based analogues. We further confirm that they are also the universal driving force for the ultrahigh Li^+ conductivities in both anion-substituted Li-poor ($Li_{6-a}PS_{5-a}X_a$, X = Cl and Br) and cation-substituted Li-rich argyrodite (e.g., $Li_{6+a}Ge_aP_{1-a}S_5I$ and $Li_{6+a}Si_aSb_{1-a}S_5I$). It is expected this strategy can be generally adopted to improve the ionic conductivity of the broad family of Li-rich argyrodite and beyond.
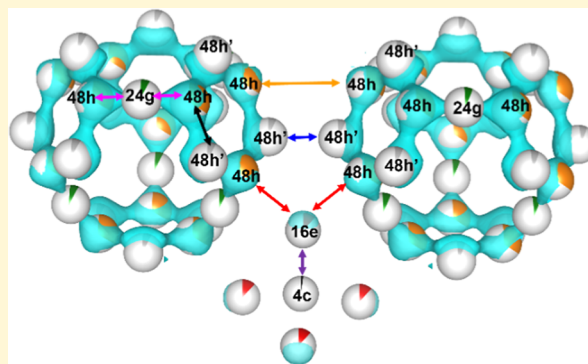
INTRODUCTION

Li^+-conducting solid electrolytes play the key role in all-solid-state Li-ion batteries that offer the potential for higher energy density and improved safety as next-generation energy storage devices.[1] Among the wide spectrum of solid electrolytes,[2] researchers draw particular attention to the thiophosphate-based Li-argyrodite (Li_6PS_5X, X = Cl, Br, or I)[3,4] owing to facile processability,[5,6] acceptable electrochemical stability,[7−9] and their competitive Li^+ conductivity ($\geq$1 mS/cm at r.t.).[3,10,11] Due to the vast compositional space of Li-argyrodite,[12−15] the Li^+ conductivity has managed to increase above 10 mS/cm at r.t.[16−20] Such dramatical enhancement in Li^+ conductivity raises an intuitive question: what is the origin of fast Li^+ conduction in Li-argyrodite?

γ-Argyrodite Li_6PS_5X (X = Cl, Br, and I) crystallize in space group $F\bar{4}3m$, with lattice parameter increases with the increase of the ionic radii of halogen anion (from Cl to I). There are four isolated $PS_4^{3−}$ units in one unit cell, which are connected with corner-, edge-, and face-shared $Li(S/X)_4$ tetrahedra, as can be seen in Figure 1. While $S^{2−}$ on the 16e sites are shared between PS_4 and $Li(S/X)_4$ tetrahedra, the two halide or halide/sulfur mixing sites (4a and 4d) are solely bonded to Li^+. Among the six plausible positions on which the $Li^+(S^{2−}/X^−)_4$ tetrahedra can reasonably locate in the γ-argyrodite[21] (Figure 1), three positions have been broadly reported except for the 16e′ site (type 1: face-sharing with one $PS_4^{3−}$ unit), 4c site (type 3: corner-sharing with four $PS_4^{3−}$ units), and 16e site (type 4: face-sharing with four $PS_4^{3−}$ unit). In general, 48h (for Cl and Br analogues) or 24g (for I analogue) site (type 5 or 5a: face-sharing double tetrahedra) secured the majority of Li^+ population, forming the backbone of the Li-cages (Figures 1 and 2).[10,11,22] 4c (type 3) site and 48h′ site (type 2: edge-sharing with one $PS_4^{3−}$ unit) have recently been proposed/identified based on Rietveld refinements[20,23] and maximum entropy method (MEM) analysis[15] of neutron powder diffraction (NPD) data in γ-argyrodite with various chemical compositions. On the other hand, a temperature-dependent (150−350 K) NPD study[24] revealed that Li^+ can also occupy the 48h′ site (type 2) even in the absence of "excess" Li^+, e.g., in Li_6PS_5Cl. While these reports[20,22,24] highlight the function of the 48h′ site (type 2) and support the idea[4] that the cage-to-cage Li^+ jump may be achieved by the 48h−48h′−48h′−48h migration pathway (type 5−type 2−type 2−type 5, Figure 2), relatively little is known about the potential contribution of the interstitial 16e sites (type 4) to the Li^+ migration (Figures 1 and 2), despite some very recent bond valence sum (BVS) analysis on this site.[25]

Pioneering works, experimentally[10,17] and computationally,[22,26] proposed that the fast Li^+ conduction in Li-argyrodite is strongly correlated with the degree of anion site-disorder,
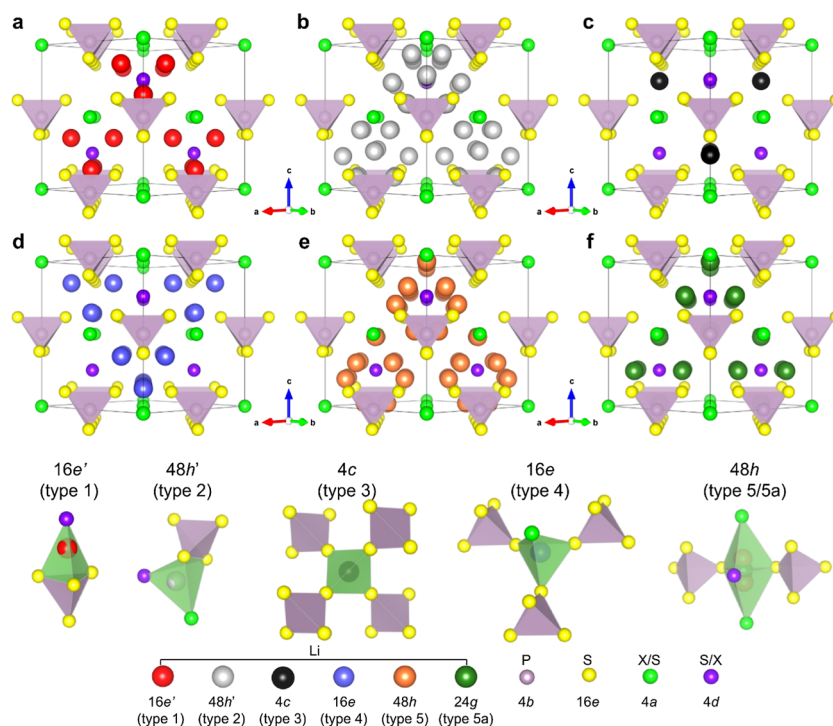
Figure 1. Crystal structure of Li-argyrodite (Li_6PS_5X, X = Cl, Br, and I). All possible lithium positions (48h, 48h′, 24g, 16e′, 16e, and 4c) are shown in (a−f). For clarity, local Li^+ environments are individually displayed in the bottom panel for each position. Note that the 24g (type 5a) site sits on a trigonal plane in between two 48h (type 5) sites.
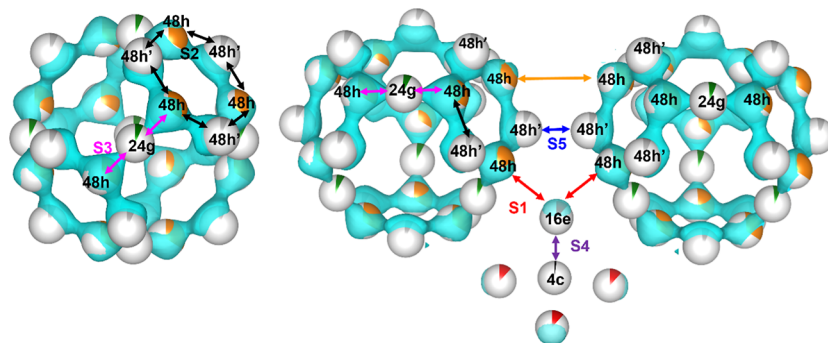
Figure 2. Plausible Li^+ migration pathways in Li-argyrodite. (Left) Intracage Li^+ migration is connected through the intracage 48h−48h′ jump (black arrow) and the doublet 48h−24g−48h jump (pink arrow). (Right) Broadly proposed direct intercage 48h′−48h′ jump and 48h−48h jump are shown in blue and orange arrows, respectively. The currently proposed intercage 48h′−16e−48h′ jumps are shown in red arrows. The potential Li^+ jump between the 16e site and 4c site is shown in purple. The cyan iso-surface represents the residual Li scattering length densities obtained from Fourier difference map (FDMs) ($F_{obs} − F_{calc}$, threshold of −0.085 fm/Å^3) calculation of Li_6PS_5Cl (against neutron diffraction data at 320 K). The assigned Li^+ positions are obtained from Rietveld refinement against corresponding neutron diffraction data. Lithium on the 48h (type 5), 24g (type 5a), 48h′ (type 2), 16e (type 4), and 4c (type 3) sites are shown as orange, gray, green, red, and black balls.

i.e., mixing of $S^{2−}$ and $Cl^−/Br^−/I^−$ on the Wyckoff site of 4a/4d. It is broadly believed that high degrees of anion site-disorder can facilitate fast Li^+ migration[27] by altering the energy landscape for different Li^+ sites. In addition, the concept of lattice softness[28−30] (or phonon softening)[31] was applied to explain the interplay between cationic hopping and anionic lattice dynamics. It is also worth mentioning that, despite unsettled consensus, rotational motion of the $PS_4^{3−}$ motifs via the paddle-wheel mechanism[32] was also proposed[33,34] to explain the fast Li^+ conduction in Li-argyrodite. Together, these insights collectively laid the foundation for the argument over the modes of Li^+ jumps, i.e., doublet, intra-, and intercage (vide infra), that create connected three-dimensional Li^+ migration paths in Li-argyrodite (Figure 2). While the importance of intercage Li^+ jump (Figure 2) to the overall high Li^+ conductivity in Li-argyrodite has been broadly acknowledged,[10,11] there is still a great controversy regarding the detailed intercage hopping mechanism. For instance, some reports proposed the direct hopping between 48h sites from neighboring Li-cages (orange arrow in Figure 2). More recently, experimental investigations in nominal[28] (6 Li^+ per formula unit, with the general formula of Li_6PS_5X) and Li-rich[15,20,27] (more than 6 Li^+ per formula unit) argyrodite advocated that the intercage Li^+ migration actually stems from an alternative Li^+ migration pathway via the 48h′−48h′ jump.[20,28] In addition, the previously overlooked intercage 48h−16e pathway has recently been proposed in the Li−Al−Si−S−O based argyrodite by Huang et al.[15,27] (Figure 2).
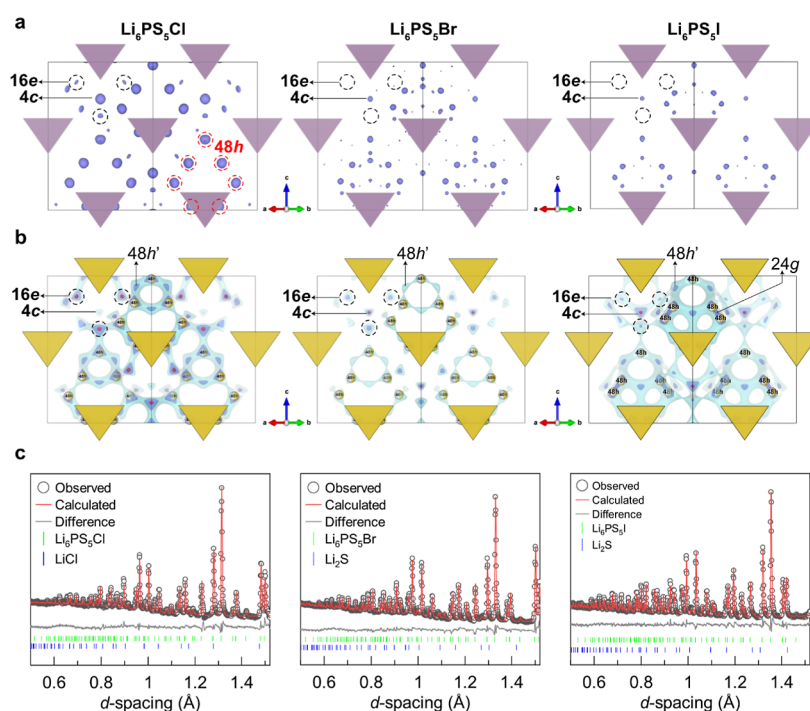
Figure 3. Determination of potential lithium positions in Li_6PS_5X (X = Cl and Br) at 100 K and Li_6PS_5I at 180 K. (a) Distribution of negative nuclear density (-0.25 fm/Å³) by MEM analysis. For simplicity, halogens are omitted and only PS_4 units are shown. Potential Li^+ sites 48h (24g), 16e, and 4c are identified. (b) Mismatch of BVS, in which three levels of iso-surface (from red to purple to blue) are shown to differentiate the energy thresholds for Li^+. The smaller the iso-surface threshold is (i.e., red), the lower the site energy is, and hence more suitable for Li^+ to occupy. (c) Rietveld refinement results of NPD data from NOMAD (Bank 5; center $2\theta = 154°$).

However, these different "inter-cage Li^+ jump" modes are often found to be strongly correlated with different anion/cation compositions. This controversy over the intercage Li^+ hopping models arose from the assignment of Li^+ to available positions (type 1−5; see Figures 1, 2 and ref 21) in the crystal structure of γ-argyrodite (S.G. $F\bar{4}3m$).[35,36]

These unsettled arguments motivate us to investigate the impact of structural attributes, e.g., Li^+ distribution, Li^+ migration paths, and their relations with anion/cation sublattices, on the mechanism of Li^+ conduction in halide substituted Li-argyrodite. Here, we employ NPD, MEM analysis, BVS calculations, electrochemical impedance spectroscopy (EIS), and ab initio molecular dynamics (AIMD) simulations to probe temperature-dependent (100−350 K) structure−property relationship in Li_6PS_5X (X = Cl, Br, or I). Particularly, the measured Li^+ conductivity is rationalized on the basis of three sites (16e, 48h′, and 48h/24g) participating in Li^+ migration within and between Li-cages. We found that (1) there is appreciable amounts of Li^+ occupancies on the 16e sites (type 4) in the nominal Li_6PS_5Cl and Li_6PS_5Br, which is accompanied by high degrees of anion site-disorder, (2) the 48h−16e−48h Li^+ jump offers a much lower migration energy pathway (relative to the previously reported direct intercage 48h−48h or 48h′−48h′ jump), leading to a much faster three-dimensional cage-to-cage Li^+ migration, and (3) Li^+ site energies and distributions can be effectively tuned by anion/cation substitution, which can be used to further increase Li^+ conductivities in halide substituted Li-argyrodite. These findings are further confirmed by both anion-substituted Li-poor ($Li_{6-x}PS_{5-x}ClBr_x$) and cation-substituted Li-rich superionic argyrodites ($Li_{6+x}P_{1-x}Ge_xS_5I$ and $Li_{6+x}Si_xSb_{1-x}S_5I$). We found that both substitution strategies can effectively regulate the relative Li^+ site energies on the 16e, 48h (24g), and 48h′

sites, leading to higher Li^+ population on the interstitial 16e site relative to their parent compounds. It also helps create more isotropic Li^+ migration pathways and hence higher overall Li^+ conductivity by reducing the average energy barriers (and their differences) among the two critical migration pathways, i.e., the intracage doublet 48h−24g−48h jump (pink arrows in Figure 2) and the intercage 48h−16e−48h jump (red arrows in Figure 2). These findings provide useful insights on how to further improve the Li^+ conductivity of the broad family of Li-argyrodite and beyond.

■ RESULTS AND DISCUSSION

Identification of Plausible Li^+ Sites. To determine the plausible Li positions (Figure 1) in Li-argyrodite with high ionic conductivity,[37−39] we employed FDMs to examine potential Li^+ sites (coherent nuclear scattering length: -1.9 fm)[40] against NPD data, and the results are presented in Figures S1−S5 and Tables S1−S3. Accordingly, potential positions, 4c site (type 3), 16e site (type 4), 48h (type 5), and 48h′ site (type 2), are observed in Li_6PS_5X (X = Cl, Br, and I), whereas the 24g site (type 5a; trigonal plane)[33] is vaguely seen in Li_6PS_5Cl or Li_6PS_5Br but becomes pronounced in Li_6PS_5I. The legitimacy of those positions is further examined by the MEM[41] analysis.

Figure 3a shows the distribution of the nuclear scattering density over 4c site (type 3), 16e site (type 4), 48h′ site (type 2), and 48h site (type 5) in Li_6PS_5X (X = Cl, Br, and I) by MEM analysis. Several features are observed: (1) 48h site (type 5) and 4c site (type 3) are captured in all compounds, (2) 16e site (type 4) is seen in Li_6PS_5Cl but is vacant in Li_6PS_5Br and Li_6PS_5I, and (3) 48h′ site (type 2) is barely observable in all compounds. While our MEM result
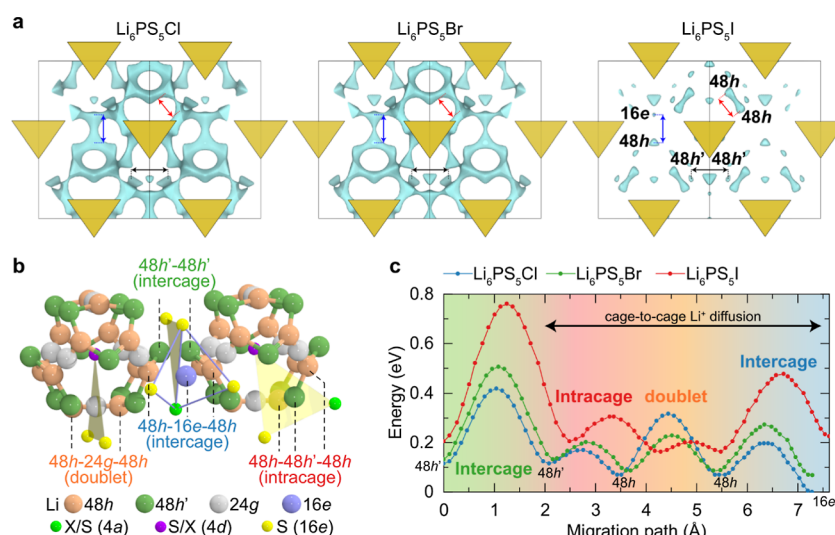
Figure 4. Li$^+$ migration paths in Li-argyrodite. (a) BVSE landscapes of Li$_6$PS$_5$Cl (100 K), Li$_6$PS$_5$Br (100 K), and Li$_6$PSI (180 K). The BVSE landscape is shown at an isosurface value of -1.87 eV for all. Red, blue, and black arrows represent the 48h–48h doublet, 48h–16e intercage, and 48h′–48h′ intercage jump, respectively. (b) Illustration of four Li$^+$ jumping modes and their migration pathway bottlenecks in Li-Argyrodite. (c) Li$^+$ migration energies as a function of migration paths. The length of migration paths in three compounds is slightly different due to different lattice parameters.

qualitatively echoes with the variations in free enthalpies of these potential sites obtained by MD simulations,[21] it provides a stark contrast to the available sites to Li$^+$ from the experimental point of view. This observation enforces us to verify the authenticity of the 4c site (type 3) and 16e site (type 4) in case they are mistakenly considered potential positions for Li$^+$. Therefore, calculations of bond valence site energy (BVSE),[42,43] which is a useful tool for searching hidden positions by predicting the energy landscape of mobile cations,[44−46] are conducted.

The 16e site (type 4) in Li$_6$PS$_5$Cl is considered a reasonable position for Li$^+$ because it has the lowest site energy (cf. red iso-surface) (Figure 3b). Accordingly, the tendency toward finding Li$^+$ on the 16e site (type 4) attenuates in the order of Li$_6$PS$_5$Cl > Li$_6$PS$_5$Br > Li$_6$PS$_5$I (see also Figure S6 for temperature dependency). In contrast, the 4c site (type 3) has lower site energy in Li$_6$PS$_5$Br and Li$_6$PS$_5$I than in Li$_6$PS$_5$Cl. The opposite trend in altering the preference for Li$^+$ to take up the 4c site (type 3) or the 16e site (type 4) is likely due to the effect of anion site-disorder on the 4a/4d site (Figure 1) and differences in the unit cell dimensions. These results are similar to the situation where the Li$^+$ density on the 24g sites (type 5a; *single position*) grows at the expense of Li$^+$ occupancy on the 48h site (type 5; *split positions*) in Li$_{6+x}$P$_{1−x}$Ge$_x$S$_5$I.[17] Turning to the 48h′ sites (type 2), the predicted site energy is the highest among all four positions (4c, 16e, 48h′, and 48h; Figure S6), confirming its metastability.

The growing evidence gathered from the FDMs, MEM analysis, and BVSE of Li$_6$PS$_5$X (X = Cl, Br, and I) eventually led us to assign Li$^+$ to four (4c, 16e, 48h′, and 48h) tetrahedra and one (24g) trigonal plane environments using the Rietveld refinement against our NPD data (Figure 3c). The fit quality is examined by R_{wp} (Table S4), and it shows that the Li$^+$ sublattice in Li$_6$PS$_5$X (X = Cl and Br) is better described with the 48h′ site (type 2), 48h site (type 5), and the previously overlooked 16e site (type 4). The Li$^+$ occupancies are found to be very small on 4c and 24g sites for both Br and Cl analogues. In accord, these positions have been identified in

monovalent Cu- and Ag-argyrodite;[47,48] therefore, our results show that the Li$^+$ distribution in Li$_6$PS$_5$Cl and Li$_6$PS$_5$Br is more complex than what was previously perceived.[16,18−20,27,28] For Li$_6$PS$_5$I, however, the 48h site (type 5) and 24g site (type 5a) together are, in line with literature,[10] sufficient to yield the best fit. Notably, there are also small amounts of Li$^+$ on the 4c site (type 3) in Li$_6$PS$_5$I.

Understanding the Li$^+$ Migration Pathway. To examine the function of the interstitial 16e site (type 4) to diffusion mechanisms, Li$^+$ migration paths and their projected energy barriers in in Li-argyrodite are studied using the BVSE landscape.[44−46] As shown in Figure 4a,b, the BVSE landscapes of Li$_6$PS$_5$X (X = Cl, Br, and I) indicate that the cage-to-cage Li$^+$ migration pathways are connected in Li$_6$PS$_5$Cl and Li$_6$PS$_5$Br with reasonably low energy barriers. In contrast, Li$_6$PS$_5$I merely conducts Li$^+$; the movement of Li$^+$ is mainly connected through the 48h–24g–48h doublet jump (type 5–type 5)[10] or the 48h–48h′ (type 5–type 2) jump, both of which are confined to isolated Li-cages due to the very large energy barrier for the intercage jump (Figure 4c). More importantly, the Li$^+$ migration path that bridges Li-cages is established by the 48h–16e jump (type 5–type 4, red arrows in Figure 2) rather than the broadly proposed direct intercage 48h–48h (type 5–type5, orange arrow in Figure 2) or 48h′–48h′ jump (type 2–type 2, blue arrow in Figure 2). This motivates us to further evaluate the significance of the 16e site (type 4) for Li$^+$ migration by comparing the energy barriers for different modes of Li$^+$ jump.

In the three-lithium-model [16e, 48h′, and 48h (24g)] proposed in this work, the overall Li$^+$ hopping consists of four possible modes of Li$^+$ jump, two of which are the 48h–16e jump (red arrow in Figure 2) and 48h′–48h′ jump (blue arrow in Figure 2) that enable the cage-to-cage Li$^+$ migration (Figures 2 and 4b). However, the estimated Li$^+$ migration energy barrier of the 48h′–48h′ jump (from BVSE, which provides qualitative estimation of the migration energy barrier) exceeds that of the 48h–16e jump by ~100 meV in Li$_6$PS$_5$Cl (Figure 4c). Such a difference becomes even more substantial
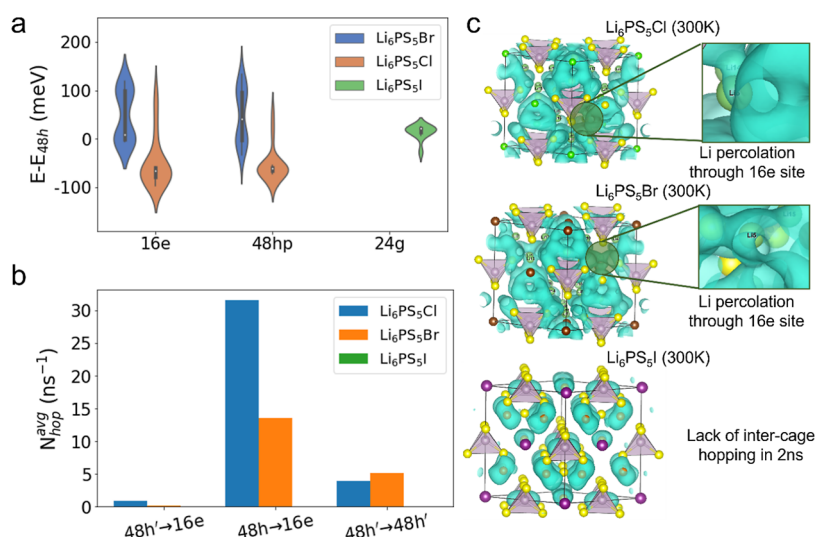
Figure 5. Probing site preference and hopping statistic by AIMD. (a) Site energy in 16e, 24g, and 48h′ with respect to 48h. (b) Statistics of number of intercage jumps at 300 K. The N_{hop}^{avg} is normalized as per Li ion and per ns. The statistics are obtained from an AIMD trajectory of 2 ns at 300 K. It should be noted that only three intercage hopping amounts are plotted in (b) as only three types of intercage hopping are observed from AIMD simulations. (c) AIMD simulation at 300 K, which shows intercage 48h−16e jump. For Cl- and Br-argyrodite, it can be clearly seen that Li diffuses (percolates) through the 16e site. In I-argyrodite, intercage hopping is absent in the simulated period of 2 ns. The Li atoms shown (green spheres) in (c) are only 16e Li sites for Cl- and Br-argyrodite. The Li atoms shown for I-argyrodite are 24g Li sites (colored in orange). Note: the hopping amounts are computed as $n_{hop} = S_{hop}/d_{hop}$. The S_{hop} here is the moving distance of Li$^+$ during the AIMD simulations, d_{hop} is the distance for each Li hop, which is approximated by the shortest Li−Li distance in a relaxed argyrodite structure.

in Li$_6$PS$_5$Br and Li$_6$PS$_5$I. Taking the intracage (48h′−48h, black arrows in Figure 2) Li$^+$ jumps into consideration, their energy barriers for Li$^+$ hopping between two adjacent sites are all inarguably smaller than the energy required for Li$^+$ to jump between two neighboring cages via 48h′ sites. Therefore, a complete cage-to-cage Li$^+$ migration can be achieved without the direct intercage 48h′−48h′ jump (Figure 4c). The evidence presented here therefore supports that the interstitial 16e site is an important saddle point to facilitate the long-range Li$^+$ migration in the Li-argyrodite. The other significant observation is that the doublet (48h−24g−48h) jump has slightly higher energy barrier (∼0.25 eV) than the intercage 48h−16e−48h jump energy barrier (∼0.21 eV) in Li$_6$PS$_5$Cl, but they are opposite in Li$_6$PS$_5$Br and Li$_6$PS$_5$I, both of which have much higher intercage jump energy barriers (Figure 4c). It is also worth pointing out that the 4c site (type 3) has much lower site energy (−0.2 eV) than the 16e site in Li$_6$PS$_5$I, and the energy barrier for the 16e to 4c jump is very small (∼0.1 eV, Figure S32). This may lead to the potential trap of interstitial Li$^+$ into the inactive 4c site (type 3, Figure 1), resulting in a much sluggish intercage Li$^+$ hopping in Li$_6$PS$_5$I. This is fully consistent with experimental observations, where the measured Li$^+$ conductivities follow the trend of Li$_6$PS$_5$Cl > Li$_6$PS$_5$Br ≫ Li$_6$PS$_5$I (see Figures S7−S11 and Tables S5, S6). Since the scanned frequency (5 MHz to 1 Hz) in impedance measurements mainly probes the long-range Li$^+$ diffusion, this result reflects that the magnitude of the highest migration energy barrier and the relative site energies is strongly correlated with the overall σ_{Li^+}. This also indicates that soft anion sublattice (Figure S11) and expanded crystal lattice (Figure S12) seem to have limited effect in improving the overall σ_{Li^+}. Instead, it suggests that different strategies are needed to improve Li$^+$ transport in the Cl/Br- and I-based Li-argyrodite: (1) for the Cl/Br-substituted analogues, decreasing the energy barrier for the intracage doublet (48h−24g−48h) pathway (pink arrow in Figure 2) while maintaining fast

intercage Li$^+$ migration through the interstitial 16e site (red arrow in Figure 2) is critical. In contrast, decreasing the energy barrier for the intercage (48h−16e−48h) jump while increasing the energy barrier between the interstitial 16e site and the inactive 4c site (purple arrow in Figure 2) is the key for achieving fast Li$^+$ transport in the I-substituted analogues (Figure 4).

Thermodynamic Origin of Li Distribution and Li$^+$ Dynamics. To understand the thermodynamic driving force for Li occupancy in 16e (type 4), 48h′ (type 2), and 24g (type 5a) sites, we have performed first-principles density functional theory calculations (DFT) on Li site energies for three sites with the reference to the situation when Li is on 48h site (type 5). We first performed electrostatic enumeration to identify the top 10 orderings with only 48h site occupied for further DFT relaxation. During the enumeration, we also enumerate the Cl/ S, Br/S, and I/S ordering following the experimental occupancy. Based on the lowest energy structure from this step (denoted as s_0), all Li atoms on 48h site are enumerated and swapped into the nearest neighboring 16e, 48h′, and 24g site, respectively (denoted as s_i). Each of the swaps will yield one additional structure for DFT relaxation. The energy difference between the reference structure s_0 and s_i, with a collection of site energy differences, leads to the violin plot shown in Figure 5a. It can be inferred from Figure 5a that both 16e sites and 48h′ sites give reasonable energetics compared with the 48h site, suggesting that the simultaneous occupancy of 16e, 48h′, and 48h sites is reasonable at room temperature. The thermodynamic driving force is even more pronounced for Li$_6$PS$_5$Cl, as negative $E − E_{48h}$ is observed for 16e and 48h′ sites. On the other hand, for Li$_6$PS$_5$I, the 24g site will be energetically more favorable, as shown by the close energetics in Figure 5a. In summary, our DFT calculations of Li$^+$ site energies in Li$_6$PS$_5$X (X = Cl, Br, and I) agree well with the BVSE analysis and the structure refinement results.
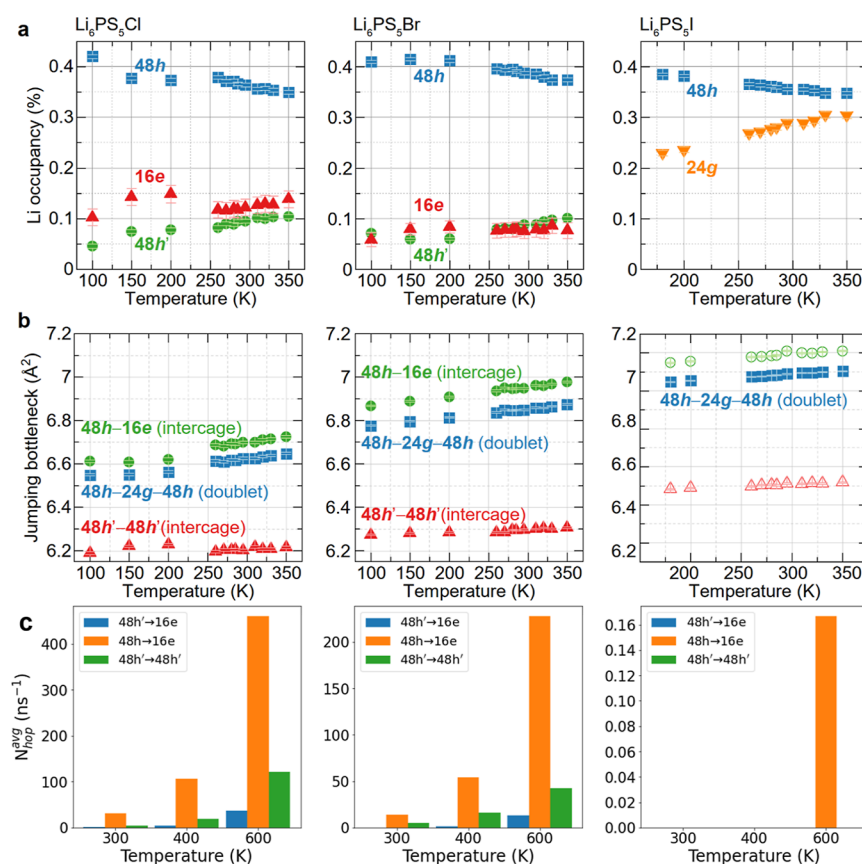
Figure 6. Temperature-dependent structural evolution of Li_6PS_5X (X = Cl, Br, and I). (a) Li^+ distribution over four crystallographic sites (16e, 24g, 48h', and 48h) derived from neutron diffraction data. (b) Li^+ jumping bottleneck areas through 48h−16e and 48h'−48h' intercage, and 48h−24g−48h doublet migration paths derived from neutron diffraction data. Open symbols in L_6PS_5I indicate a virtual case with computed areas assuming Li^+ occupies 16e and 48h' sites. (c) Hopping rates vs different migration mechanisms (from AIMD).

The kinetic process of Li^+ migration in Li_6PS_5X (X = Cl, Br, and I) is then investigated using the experimentally refined Li^+ and halogen occupancies (Figure 5b,c) and with AIMD simulations. Room temperature (300 K) AIMD simulations are performed to obtain the simulated Li migration pathway to be compared with neutron diffraction observations. AIMD simulations for 2 ns are performed to make sure we have enough statistics for hopping for good conductors Li_6PS_5Cl and Li_6PS_5Br. As shown by Figure 5b, the average amount of hopping through 48h' → 16e, 48h → 16e, and 48h' → 48h' are extracted separately from the AIMD simulations. It can be reflected by Figure 5b that for both Li_6PS_5Cl and Li_6PS_5Br, a large number of the intercage jumps occur through 48h → 16e path rather than through 48h' → 48h'. On the other hand, Li_6PS_5I shows much lower ionic conductivity so that no intercage jump is observed. The percolation of Li through 16e can further be supported by visualizing the Li^+ probability distribution extract from the 2 ns trajectory of AIMD simulations in Figure 5c. For both Li_6PS_5Cl and Li_6PS_5Br, very significant Li^+ probability density can be observed, which is absent in Li_6PS_5I. The AIMD simulations thus confirm the experimental observations and support the argument that Li^+ intercage diffusion through 48h → 16e is actually a pronounced mechanism at room temperature.

Effect of Structural Attributes on Li^+ Conductivity. *Li^+ Distribution.* Following the results discussed in the first section, we employed the three-lithium-site model (16e, 48h', and 48h) in the Rietveld refinement to assess the temperature-

dependence of Li^+ distribution in Li-argyrodite (Figure 6a). While the occupancy of Li^+ on 48h site decreases with increasing temperature, an opposite trend is found with 16e and 48h' sites. In addition, Li^+ preferably occupies the 16e site and its occupancy is greater in Li_6PS_5Cl than in Li_6PS_5Br. For the 24g site, large occupancies are observed in Li_6PS_5I but barely present in the Cl and Br analogues, presumably due to expanded crystal lattice ($Li_6PS_5I > Li_6PS_5Br > Li_6PS_5Cl$).[10] These findings resonate with the AIMD simulations (see also Figures S14−S7), and it further stresses the importance of the 16e site in promoting fast Li^+ conduction (cf. Figures 4 and 5).

The distinctive distribution of Li^+ in Li_6PS_5X (X = Cl, Br, and I) can be further understood, in addition to considering the size of Li-cages (see Figure S18),[24] by examining the average ratio of inter- and intracage jumping distance (D_{inter}/D_{intra}) (see Experimental Section), which reflects the overall Li^+ migration energy landscape. In fact, D_{inter}/D_{intra} was employed to characterize Na-argyrodite and it was found that fast Na-ion conduction can be computationally achieved when $D_{inter}/D_{intra} \approx 1$.[49] Intuitively, the variations in D_{inter} and D_{intra} are believed to be halogen-dependent—in other words, the distribution of different anions (X^- or S^{2-}) on 4a/4d sites and its attraction toward Li^+ play a pivotal role in modifying the D_{inter} and D_{intra}. However, it should also be stressed that the unit cell dimensions, and bonding environments are similar for the framework (particularly the high valent cations bonded to S^{2-}, e.g., P^{5+} in PS_4^{3-} motifs). Since Li-cage$_{4a}$ and Li-cage$_{4c}$ are directly connected, the most favorable condition for Li^+

migration can be achieved when there is equal jumping distances between the two neighboring cages, i.e., $D_{inter}/D_{intra} \sim 1$. In this scenario, both Li-cage$_{4a}$ and Li-cage$_{4d}$ are expected to present similar sizes with comparable Li$^+$-(4d/4a) distances.

Li$^+$ Jumping Pathway Bottleneck. Figure 6b illustrates the temperature-dependent Li$^+$ migration pathway bottlenecks. A larger area of the saddle point is observed in the 48h−16e path than that in the 48h′−48h′, indicating that the former intercage jump may better facilitate the Li$^+$ migration. Besides, we notice that the Li$_{48}$h′(S/X)$_4$ tetrahedron is markedly more distorted than the Li$_{16e/48h}$(S/X)$_4$ one (Figure S19). This finding implies that the deviation from the ideal geometry of a tetrahedron could be another factor that imposes a structural constraint to restrict the 48h′−48h′ intercage Li$^+$ jump. Notably, although the Li$^+$ jumping cross-section for the 48h−16e path in Li$_6$PS$_5$Br expands more than in Li$_6$PS$_5$Cl, Li$_6$PS$_5$Cl still outperforms Li$_6$PS$_5$Br on σ_{Li^+} (Figure S7). Likewise, the same argument holds true for Li$_6$PS$_5$I assuming that Li$^+$ virtually occupies the 16e and 48h′ sites. This suggests that the ideal Li$^+$ jumping bottleneck depends on the specific halide anion and site energies of different Li$^+$ interstitial sites. The absolute values of the areas of the jumping bottleneck areas are not directly related to the energy barriers. Additionally, we have performed −ICOHP calculations for Li−X interaction within Li$_6$PS$_5$X (X = Cl, Br, and I). As shown by Figure S20, there is no obvious difference among the −ICOHP values for three types of argyrodite, suggesting that the halogen-dependent Li distribution is majorly a strain (lattice dimension)-induced phenomenon, which is less relevant to the electronic structure of X$^-$/S^{2-} ions. Taken together, this suggests that reducing the energy differences between the 48h and 16e sites while simultaneously maintaining an appropriately sized bottleneck for the 48h−16e jump seems to be one of the key factors for realizing fast Li$^+$ migration in Li-argyrodite. This argument is further supported by the AIMD simulations (Figure 6c) and BVSE calculation (Figure 4c). This result indicates that the 48h−16e hopping dominates the intercage Li$^+$ migration for Cl- and Br-based argyrodite. In contrast, the AIMD simulation found that there is very limited intercage hopping for I-based argyrodite even at 600 K, which indeed shows much lower σ_{Li^+} relative to the Cl and Br analogues.

Tuning Li$^+$ Distribution is the Key to the Promotion of Fast σ_{Li^+} in Li-Argyrodite. The abovementioned neutron diffraction, BVSE calculation, and AIMD simulation results suggest that the intercage 48h−16e−48h Li$^+$ migration pathway plays a pivotal role in promoting fast Li$^+$ transport. Since Li$^+$ on 48h (type 3) and 16e (type 1) sites are bonded to three S^{2-} (corner shared with PS$_4$ tetrahedra) and one anion (halide or S^{2-}) on the 4a or 4d site, it is expected that the site energy differences between the 48h and 16e sites will highly depend on anion environments on the 4a/4d sites, i.e., the types of anions and the Li-anion bonding distances. In this section, we will show that a few commonly implemented strategies to improve Li$^+$ conductivity are universally achieved by tuning the Li$^+$ distributions on different interstitial sites, particularly those on the 48h and 16e sites. This redistribution can not only result in fast intercage Li$^+$ migrations via the newly discovered 48h−16e−48h pathway, but also lead to flatter intercage and intracage migration energy landscape.

One common strategy to improve the Li$^+$ conductivity in Li-argyrodite is by substituting S^{2-} with halogen anions (Cl$^-$ or Br$^-$), forming Li-poor Li$_{6-a}$PS$_{5-a}$X$_{1+a}$ (X = Cl or Br).

Particularly, dramatic improvement of Li$^+$ conductivity has been reported in the mixed halogen-substituted Li$_{6-a}$PS$_{5-a}$ClBr$_a$.[50] Other than the increased carrier (vacancy) concentration (due to the creation of Li$^+$ vacancy), we found that this type of substitution can also dramatically lower the energy barriers for both intracage doublet 48h−24g−48h jump and intercage 48h−16e−48h jump (Figures S22 and S23). We also found that from the structure point of view, this approach is realized by increasing the Li$^+$ occupancies on the interstitial 16e site and achieving equal intercage and intracage Li$^+$ jumping distances ($D_{inter}/D_{intra} \sim 1$).

Here, we use Li$_{5.7}$PS$_{4.7}$ClBr$_{0.3}$ as an example (which is chosen because phase pure sample can be synthesized without large amounts of impurities and the relatively small increase of the Li$^+$ vacancy concentration, Figure S22) to demonstrate the effectiveness of this approach. By sacrificing a small portion of Li$^+$ on the 48h site (Figure 7a), the occupancy of Li$^+$ on the
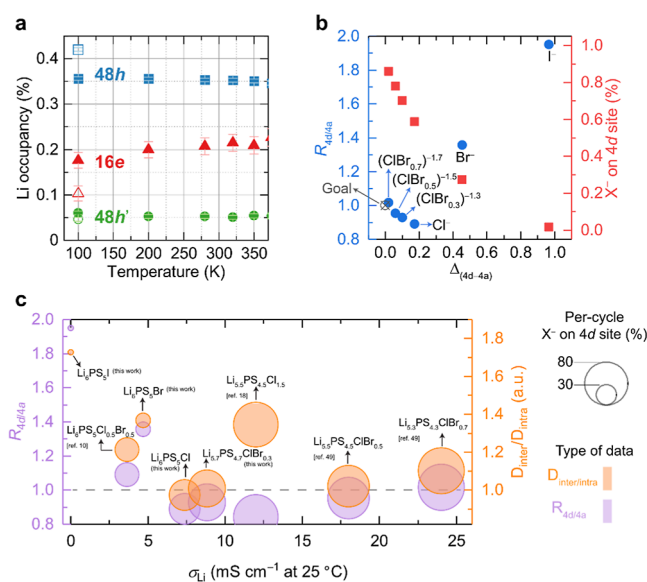
Figure 7. Demonstration of the importance of the interstitial 16e site and equal intercage and intracage jumping distances in promoting fast Li$^+$ transport in Cl- and Br-based Li-argyrodite. (a) Temperature-dependent Li$^+$ occupancy in Li$_{5.7}$PS$_{4.7}$ClBr$_{0.3}$ derived from the Rietveld refinement against NPD data. The Li$^+$ occupancy in Li$_6$PS$_5$Cl at 100 K (open symbols) is added for comparison. Much higher Li$^+$ occupancies on the interstitial 16e site have been observed in Li$_{5.7}$PS$_{4.7}$ClBr$_{0.3}$ relative to the parent compound. (b) Correlation of negative charge distribution (ratio $R_{4d/4a}$ and difference Δ_{4d-4a}) with X$^-$/S^{2-} disorder on the halide substituted Li-argyrodites. (c) Correlation of Li$^+$ conductivity with $R_{4d/4a}$ and D_{inter}/D_{intra}. Reported data from literature[10,18,49] are added for comparisons. It should be noted that both carrier concentration and the redistribution of Li$^+$ can affect the overall σ_{Li^+}.

16e site (type 4) increases relative to the parent Li$_6$PS$_5$Cl. By contrast, the increase in Li$^+$ density for the 48h′ site (type 2) is marginal when taking errors into consideration. The increased disorder (~70%) in Li$_{5.7}$PS$_{4.7}$ClBr$_{0.3}$ can be statistically quantified by summing individual contribution from Cl$_{0.6}^-$ + Br$_{0.1}^-$ over S$_{0.3}^{2-}$ on the 4d site (Figure 7b). More importantly, the negative charge ratio ($R_{4d/4a}$) turns closer to 1, and the difference in the negative charge (Δ_{4d-4a}) reduces further to 0.1. Similarly, an almost unity of $R_{4d/4a}$ can be achieved, although it was not originally documented in a recent work,[50] in Li$_{5.5}$PS$_{4.5}$ClBr$_{0.5}$ and Li$_{5.3}$PS$_{4.3}$ClBr$_{0.7}$ (which contains on the
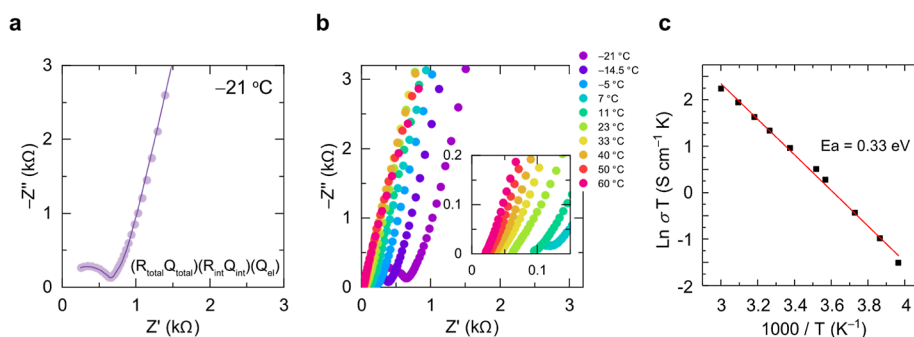
Figure 8. Li^+ conductivity in $Li_{5.7}PS_{4.7}ClBr_{0.3}$. (a) Representative Nyquist plot of $Li_{5.7}PS_{4.7}ClBr_{0.3}$ (-21 °C). (b) Temperature-dependent Nyquist plots of $Li_{5.7}PS_{4.7}ClBr_{0.3}$. The inset shows the same set of data collected at high temperatures. (c) Arrhenius plot of $Li_{5.7}PS_{4.7}ClBr_{0.3}$.

relatively large amounts of impurity phases relative to the $x = 0.3$ phase used for the current study.[50] Finally, we examine the distribution of intra- and intercage Li^+ jumping distances (D_{inter}/D_{intra}) with negative charge ratio ($R_{4d/4a}$) and their correlation with Li^+ conductivity. As shown in Figure 7c, when $R_{4d/4a}$ shifts to 1, the averaged D_{inter}/D_{intra} ratio decreases significantly. Upon slight bromination, the D_{inter}/D_{intra} ratio varies from slightly <1 in L_6PS_5Cl to ~1 in $Li_{5.7}PS_{4.7}ClBr_{0.3}$ (similar trend in $Li_{5.5}PS_{4.5}ClBr_{0.5}$ and $Li_{5.3}PS_{4.3}ClBr_{0.7}$),[25,50] indicating homogeneous Li^+ jumping distances within and across neighboring Li-cages.

The redistribution of Li^+ over 16e, 48h′, and 48h (24g) sites is central to the observed improvement of Li^+ conductivity in $Li_{5.7}PS_{4.7}ClBr_{0.3}$. A higher fraction of Li^+ on the 16e site suggests that the 16e site is more frequently accessed by Li^+ via 48h−16e jump with relatively low activation energy. Comparable change in this structural attribute, conversely, cannot be identified in other reported "mono-halide" Li-argyrodite even with high magnitude (>60%) of X^-/S^{2-} disorder on 4d site (Table S8). Indeed, this observation suggests that extensive anion site-mixing over 4a and 4d sites is not the determining factor for fast Li^+ conduction. In addition, the effect of expanding unit cell dimension on Li^+ conductivity can be minimal since only 0.3 mol of Br^- p.f.u. was employed (Figure S22e), which is also reflected in the fact that $Li_{5.7}PS_{4.7}ClBr_{0.3}$ has similar Li^+ jumping bottlenecks (Figure S22f) as those in Li_6PS_5Cl (Figure 6b).

It should be noted that the absolute degree of anion (X^-/S^{2-}) disorder is not necessarily the governing factor for fast Li^+ conductivity. For example, despite comparable extent of Cl^-/S^{2-} disorder and Li^+ vacancy concentration in $Li_{5.5}PS_{4.5}Cl_{1.5}$[18] (Tables S9 and S10), the Li^+ conductivity is much smaller than those reported in the $Li_{5.5}PS_{4.5}ClBr_{0.5}$.[50] Indeed, the Li^+ occupancy on the 16e site in $Li_{5.5}PS_{4.5}Cl_{1.5}$ is refined to be 0.12(1) (Figures S24, S25 and Table S9), much lower than that in $Li_{5.5}PS_{4.5}ClBr_{0.5}$ (0.17(1)) (Figures S26, S27 and Table S10). It is also worth pointing out that the energy differences between the intracage (doublet 48h−24g−48h) jump and the intercage (48h−16e) jump in $Li_{5.5}PS_{4.5}ClBr_{0.5}$ is much smaller than those in the $Li_{5.5}PS_{4.5}Cl_{1.5}$ (Figure S23). Taken together, these findings suggest that besides creating higher carrier concentration (Li^+ or vacancy), simultaneously increasing Li^+ occupancies on the interstitial 16e site, is a critical factor for promoting fast Li^+ transport in Cl/Br substituted Li-argyrodite. From the structure point of view, this is reflected in forming a more homogeneous intercage and intracage jumping distances (with $D_{inter}/D_{intra} \sim 1$). As a result, the room-temperature Li^+ conductivity improves from ~6 mS cm^{-1} in Li_6PS_5Cl to near

10 mS cm^{-1} in $Li_{5.7}PS_{4.7}ClBr_{0.3}$ (Figures 7c, 8, and Table S8). Further increasing the carrier concentration (e.g., Li^+ vacancies) while regulating D_{inter}/D_{intra} to unity can drastically increase the Li^+ conductivity to over 20 mS/cm (Figure 7c).[50]

Finally, we notice that cation-substituted I-based argyrodite[17,20] (Figure S28) with negligible I^-/S^{2-} disorder also shows very high Li^+ conductivity (Figure S29 and Table S11). These Li-argyrodites[17,20] typically have cation mixing occurs on the 4b site involving the replacement of P^{5+} with Si^{4+}, Ge^{4+}, and/or Sb^{5+}. This cation substitution modifies the local environment of the original PS_4^{3-} units, which in turn affects the site energies of different Li interstitial sites and hence affects the neighboring Li^+ distribution. Particularly, those on the 48h site and 16e site have noticeable changes after introducing cation substitution. Here, we use $Li_{6.5}Sb_{0.5}Si_{0.5}S_5I$ as an example to demonstrate the importance of tuning Li^+ distribution on the interstitial sites, particularly on the 16e site, in promoting Li^+ conductivity. The refined structure of $Li_{6.5}Sb_{0.5}Si_{0.5}S_5I$ is shown in Figures S30, S31, and Table S12. The refined Li site occupancy on the 16e site is 0.12(1). The estimated energy barriers (from BVSE) for the 48h−16e jump decrease from ~0.3 eV in Li_6PS_5I to ~0.25 eV (Figure S32) in $Li_{6.5}Sb_{0.5}Si_{0.5}S_5I$, leading to a lower Li^+ hopping energy barrier in this cation substituted compound. More importantly, the cation substitution dramatically increases the estimated migration energy barrier between the 16e site and the 4c site (Figure S32), effectively preventing entrapment of Li^+ in the inactive 4c site (purple arrow in Figure 2) during the intercage jump. This increase of the energy barrier between the 16e site and the inactive 4c site also confines the overall Li^+ hopping to those among the intracage doublet 48h−24g−48h jump, 48h−48h′ jump, and the intercage 48h−16e−48h jump, leading to a flattened energy landscape for Li^+ migration (Figures S23 and S32). As a result, similar to the Cl- and Br-based argyrodites, this flattened energy landscape is also reflected in the formation of more uniform distribution of intercage and intracage jumping distances, i.e., with $D_{inter}/D_{intra} \sim 1$ (Figure S28). Almost identical structure features have also been found in the Ge-substituted $Li_{6.6}Ge_{0.6}P_{0.4}S_5I$ (Figures S32−S34 and Table S13). Lastly, it is worth pointing out that noticeable amounts of halide vacancies (I^-) are refined on the anion 4d site (Tables S12 and S13) in these cation-substituted argyrodites, while the anion 4a sites are found to be fully occupied by S^{2-}. The presence of halide vacancies on the 4d site is expected to play an important role in increasing Li^+ occupancies on the 16e site (which is an interstitial site with very high site energy in the parent compound, Li_6PS_5I). Further theoretical investigation, similar to the work by Gorai

et al.,[51] is needed to understand how these halide vacancies on the 4d site affect the overall Li^+ transports.

CONCLUSIONS

Through a variety of structure analysis (FDM, MEM, and BVSE) and computational (DFT and AIMD) tools, we clarified the role of Li^+ site distribution and its effect on Li^+ migration in Li-argyrodite. We found that the promotion of Li^+ conductivities is strongly correlated with a previously over-looked Li^+ interstitial site (16e), which is critical for realizing the fast intercage Li^+ migration. A more isotropic Li^+ migration pathway ($D_{inter}/D_{intra} \sim 1$) and higher Li^+ occupancies on the interstitial 16e site are found to be critical factors for achieving high Li^+ conductivity in Li-argyrodite. These findings provide useful insights to further improve the ionic conductivity of the broad family of Li-argyrodite and beyond. They also highlight the importance of lithium sublattice engineering in promoting fast Li^+ conductivity.

EXPERIMENTAL SECTION

Synthesis. We performed the synthesis of Li-argyrodite following literature.[16] In this work, Li_6PS_5Cl, Li_6PS_5Br, Li_6PS_5I, $Li_{5.5}PS_{4.5}Cl_{1.5}$, $Li_{5.7}PS_{4.7}ClBr_{0.3}$, $Li_{6.5}Si_{0.5}Sb_{0.5}S_5I$, $Li_{6.6}Si_{0.6}Sb_{0.4}S_5I$, $Li_{6.2}Ge_{0.2}P_{0.8}S_5I$, $Li_{6.4}Ge_{0.4}P_{0.6}S_5I$, and $Li_{6.6}Ge_{0.6}P_{0.4}S_5I$ were synthesized. Depending on compositions of Li-argyrodite, a stoichiometric mixture of Li_2S (Sigma-Aldrich, 99.99%), P_2S_5(Macklin, 99%), LiCl (Macklin, 99%), LiBr (Macklin, 99%), LiI (Macklin, 99%), Si (Sigma-Aldrich, 99%), Sb_2S_3 (Sigma-Aldrich, 99.995%), and GeS_2 (Kojundo, 99.99%) were placed in an argon-filled zirconia jar (25 mL in volume) with zirconia balls (12 mm in diameter). The mixture was mechanically milled using a planetary ball mill apparatus for 5 h at a rotating speed of 550 rpm. After that, the as-mixed precursors were sealed in a glass tube in vacuum and transferred to a quartz tube furnace for heat treatment that was first heated to 300 °C with a ramp of 5 °C min^{-1}, then maintained at 300 °C for 12 h, and cooled down to room temperature. Last, the product was heated to 500 °C with a ramp of 5 °C min^{-1}, maintained at 500−550 °C for 12 h, and cooled down to room temperature. After sintering, pellets of Li-argyrodite were cracked into powders for neutron diffraction experiments. Sample handling was conducted under Ar (Mbraun, H_2O < 0.5 ppm, O_2 < 0.5 ppm).

Neutron Powder Diffraction. Time-of-flight (TOF) neutron diffraction patterns of Li-argyrodite were acquired at the NOMAD (BL-1B) at the Spallation Neutron Source at Oak Ridge National Laboratory. Each powdered sample (∼300 mg) was sealed into a 3 mm quartz capillary. Four 24 min scans were collected at each temperature points (from 100 to 350 K) and then summed to improve the statistics. The background signal (empty quartz) was subtracted from multibank neutron diffraction data, which then were normalized against the scattering signal from a 6 mm vanadium rod.

The Rietveld refinement was performed in TOPAS (v6).[52] The d-spacing of TOF neutron powder patterns (NPDs) was computed by TOF = zero + Difc*d + Difa*d^2. Zero and Difc were obtained by refining the NPD of the NIST standard Si 640e and then fixing them as constants. Difa was open for refinement in all four banks (#2 to #5) to account for sample displacements and peak shifts induced by absorption. Absorption correction was made by employing an empirical Lobanov formula.[53] Peak profiles for low-resolution banks (#2 and #3) were described by a convolution of a back-to-back exponential function and a symmetrical Gaussian function. For high-resolution banks (#4 and #5), modified Ikeda−Carpenter−David function was employed to compute the moderator-induced peak profiles. The reported structure of $Li_6PS_5I^3$ (S.G. $F\bar{4}3m$) was constructed as the starting model for refinements. Anionic sublattice composed of P^{5+}, $S^{2−}$, and $X^−$ (Cl, Br, and I) was first refined over site occupancies and isotropic atomic displacement (B_{eq}) parameters at 100 K (Li_6PS_5Cl, Li_6PS_5Br, and $Li_{5.7}PS_{4.7}ClBr_{0.3}$) or 180 K ($Li_6PS_5I$);

below 180 K, Li_6PS_5I experiences phase transition from cubic phase (S.G. $F\bar{4}3m$) to monoclinic phase (S.G. Cc).[21] Then, Li^+ was tentatively assigned to only the Wyckoff site of 48h (since it is the most favorable position as suggested by MD simulaitons[5]), in which, step-by-step, the atomic coordinates, the site occupancies, and the isotropic atomic displacement parameters were refined. The FDM ($F_0 − F_c$) was examined at this stage to seek potential Li^+ positions by visualizing the residual negative nuclear density in TOPAS (v6). To enhance the confidence of the Li^+ position assignments (i.e., 16e and 48h′), the refined structure was also examined using MEM and BVS, both of which are capable of identifying the potential Li^+ positions despite different working principles. After assigning Li^+ to all the possible positions, all the structural parameters were refined at the same time and no unrealistic results were detected (e.g., negative atomic displacement parameters). The quality of the Rietveld refinement was assessed by R_{wp} and GoF (goodness-of-fit). Constraints that were applied to lithium positions, site occupancies, and isotropic atomic displacement parameters are shown in Tables S1 and S2. It should be noted that the fit indicator, R_{wp}, responds to the Li^+ position assignments, in which a reduction of R_{wp} is observed if Li^+ resides at appropriate positions (see Table S3).

The inter- and intracage $Li^+−Li^+$ distance (noted as D_{inter} and D_{intra}) was calculated based on the refined structure against NPD results. 48h−16e path and 48h′−48h′ path are considered intercage jump, whereas 48h−48h path (through 24g) and 48h−48h′ path are considered intracage jump. A Detailed definition of intercage and intracage jump can be found in Figure 2. Each type of jumping was counted, and then the weighted averaged values were computed. The distribution of jumping distances was characterized as D_{inter}/D_{intra}.

Electrochemical Impedance Spectroscopy. For the variable temperature AC impedance measurements, the as-synthesized Li-argyrodite powders were pelletized at 3 tons and then sandwiched in between two pieces of indium foils in a home-built PEEK cell. The PEEK cell was then hand tightened before measurements. Variable-temperature AC impedance measurements were carried out on a Gamry Reference 600$^+$ from −27 to 60 °C in a frequency range from 5 MHz to 1 Hz under a perturbation of 50 mV. The contact area and thickness used for converting impedance to conductivity was 0.173 cm^2 and 0.1 cm. Additional room temperature (25 °C) AC impedance measurements (for Li_6PS_5Cl, Li_6PS_5Br, $Li_{5.5}PS_{4.5}Cl_{1.5}$, $Li_{6.6}Si_{0.6}Sb_{0.4}S_5I$, and $Li_{6.6}Ge_{0.6}P_{0.4}S_5I$) were carried out using steel blocking electrodes to mitigate the potential interfacial impedance contributions. Fifteen ∼20 MPa pressure was applied during the room temperature EIS measurements. The analysis of EIS data were performed on a Gamry Echem analyst and Biological EC-Lab. The EIS data (<25 °C) were analyzed with the equivalent circuit $(R_{total}Q_{total})(R_{interface}Q_{interface})(Q_{el})$, where the subscripts total, inter-face, and el refer to total resistance (grain and grain boundary), Li−In interface, and blocking electrodes. Instead of using capacitor (C), the constant phase element (Q) was employed in the equivalent circuit to represent the nonideal behavior of EIS spectra. Also, the contribution of the Li−In interface was added to accommodate the interfacial decomposition,[2] which was not the main interest in this work. At T > 25 °C, inductance (L) was introduced, and the equivalent circuit was simplified to $(L)(R_{total}Q_{total})(Q_{el})$. In general, the order of Li^+ conductivity follows $Li_{5.7}PS_{4.7}ClBr_{0.3}$ > Li_6PS_5Cl > Li_6PS_5Br ≫ Li_6PS_5I. $Li_{5.5}PS_{4.5}Cl_{1.5}$, $Li_{6.6}Si_{0.6}Sb_{0.4}S_5I$, and $Li_{6.6}Ge_{0.6}P_{0.4}S_5I$ all showed very high room-temperature Li^+ conductivity (>10 mS/cm, see Table S13).

Electrochemical Stability Window Tests. The stability of Li_6PS_5X (X = Cl, Br, and I) during oxidation and reduction processes was investigated with cyclic voltammetry (CV) measurement. The Li_6PS_5X/Super P carbon black (70/30 in weight ratio) mixture was ball-milled in a rotating speed of 200 rpm and worked as a cathode material. In brief, 200 mg of Li_6PS_5X powder was cold-pressed into a pellet under 360 MPa, and 10 mg of the as-prepared cathode was cast onto the pellet with a pressure of 180 MPa. Finally, 30 mg of the Li−Si anode was pressed onto the other side of the pellet with a pressure of 360 MPa to form solid-state cells. CV curves were performed on

the solid-state cell at a scan rate of 0.5 mV s^{-1} in a range of 0.5–4.5 V (vs Li–Si).

Fabrication and Test of All-Solid-State Li Metal Battery. For the cathode, LiCoO$_2$, Li$_6$PS$_5$X (X = Cl and Br), and Super P carbon black were mixed at the weight ratio of 70/30/0.3 in a stainless steel jar. The mixture was then mechanically milled for 1 h at a rotating speed of 200 rpm. Then, 200 mg of solid electrolyte powder was pressed into a pellet with a diameter of 10 mm under 360 MPa. 8 mg of the as-prepared cathode was pressed onto the pellet, and 30 mg of the Li–Si anode was pressed onto the other side. The mass loading of LiCoO$_2$ was 7.13 mg cm^{-1}. To fully utilize LiCoO$_2$, an activation process was performed at 0.1 C for the first two cycles. Cells were maintained stably for 220 cycles at 0.3 C.

Maximum Entropy Method. The distribution of nuclear density of Li-argyrodite was computed using the MEM using the zeroth order single-pixel approximation algorithm (ZSPA) in Dysnomia.[54] The input file (.mem) was prepared in Jana2006,[55] from which the neutron scattering structure factors and standard deviations were computed for the refined crystal structure generated by TOPAS (v6). The Lagrangian multiplier was 0.002, and the number of voxels in the unit cell was 128 × 128 × 128. The coefficients t and E were optimized to satisfy the constraints as documented in Dysnomia's manual.[6] The output file (.pgrid) was examined in VESTA[56] and compared with the refined crystal structure as well as the FDM and the BVSE landscape.

BVSE Analysis. The BVSE of Li-argyrodite was performed using *softBV*(v1.2).[42,43] The crystallographic information file (CIF), obtained through the Rietveld refinement of the NPD of Li-argyrodite in TOPAS, was assessed in *softBV*, and the global instability index (GII)[9] was found to be no larger than 0.22 in all refined crystal structures; hence, the validity of the CIFs was confirmed. The input file (.cube) was generated in *softBV*, and the BVSE landscape was plotted in VESTA[8] to visualize the Li-ion migration paths across 16e, 48h', and 48h site and was compared with the FDM and the distribution of nuclear density probed by the MEM analysis.

DFT Calculations and AIMD Simulations. DFT, as implemented in the plane-wave-basis-set Vienna ab initio simulation package,[57] was used to calculate the total energy of different Li-argyrodite. Projector-augmented wave potentials with a kinetic energy cutoff of 520 eV were employed in all the structural optimizations and total-energy calculations, and the exchange and correlation functionals were described using the Perdew–Burke–Ernzerhof generalized gradient approximation.[58] In order to understand the site energy difference at different identified Wyckoff positions, we have performed enumeration of different Li-vacancy and S-halogen ordering at considered materials compositions. For each examined site occupancy, we have enumerated all possible atomic ordering and picked up 20 structures with the lowest electrostatic energy for DFT calculations. For all the calculations, a reciprocal space discretization of 25 k-points per Å^{-1} was applied, and the convergence criteria were set to 10^{-6} eV for electronic optimization and 0.02 eV/Å for ionic optimization. AIMD, initialized from the lowest-energy atomic configurations, was used to investigate the ionic conductivity and kinetic evolution of site occupancy. All the AIMD calculations used an NVT ensemble with a time step of 1 fs and a Nosé–Hoover thermostat[59] with a period of 2 ns. A minimal Γ-point-only k-point grid was used with spin-polarized calculations. The AIMD simulations were run at 300, 400, and 600 K, respectively, to approximate the experimental condition.

■ ASSOCIATED CONTENT

Ⓢ Supporting Information

The Supporting Information is available free of charge at https://pubs.acs.org/doi/10.1021/acs.chemmater.3c02269.

> Additional diffraction data, structure information, AC impedance data, AIMD simulation results, BVSE maps, CV curves of related Li-argyrodites and cycling tests of all solid-state Li metal batteries, refined structures, results of equivalent circuit modeling of the impedance spectra, and extracted Li$^+$ conductivity values (PDF)

■ AUTHOR INFORMATION

Corresponding Authors
Bin Ouyang − *Department of Chemistry and Biochemistry, Florida State University, Tallahassee, Florida 32304, United States;* ⓞ orcid.org/0000-0002-8181-6815; Email: bouyang@fsu.edu

Xuyong Feng − *The Walker Department of Mechanical Engineering, The University of Texas at Austin, Austin, Texas 78712, United States; School of Materials Science and Engineering, Anhui Provincial Key Laboratory of Advanced Functional Materials and Devices, Hefei University of Technology, Hefei, Anhui 230009, P. R. China;* Email: 2021800026@hfut.edu.cn

Jue Liu − *Neutron Scattering Division, Oak Ridge National Laboratory, Oak Ridge, Tennessee 37831, United States;* ⓞ orcid.org/0000-0002-4453-910X; Email: liuj1@ornl.gov

Authors
Po-Hsiu Chien − *Neutron Scattering Division, Oak Ridge National Laboratory, Oak Ridge, Tennessee 37831, United States;* ⓞ orcid.org/0000-0002-1607-1271

Lei Dong − *School of Materials Science and Engineering, Anhui Provincial Key Laboratory of Advanced Functional Materials and Devices, Hefei University of Technology, Hefei, Anhui 230009, P. R. China*

David Mitlin − *The Walker Department of Mechanical Engineering, The University of Texas at Austin, Austin, Texas 78712, United States;* ⓞ orcid.org/0000-0002-7556-3575

Jagjit Nanda − *Chemical Sciences Division, Oak Ridge National Laboratory, Oak Ridge, Tennessee 37831, United States; SLAC National Accelerator Laboratory, Menlo Park, California 94025, United States;* ⓞ orcid.org/0000-0002-6875-0057

Complete contact information is available at:
https://pubs.acs.org/10.1021/acs.chemmater.3c02269

Notes
The authors declare no competing financial interest.

■ REFERENCES

(1) Janek, J.; Zeier, W. G. A Solid Future for Battery Development. *Nat. Energy* **2016**, *1*, 16141.

(2) Bachman, J. C.; Muy, S.; Grimaud, A.; Chang, H.-H.; Pour, N.; Lux, S. F.; Paschos, O.; Maglia, F.; Lupart, S.; Lamp, P.; Giordano, L.; Shao-Horn, Y. Inorganic Solid-State Electrolytes for Lithium Batteries: Mechanisms and Properties Governing Ion Conduction. *Chem. Rev.* **2016**, *116*, 140−162.

(3) Deiseroth, H.-J.; Kong, S.-T.; Eckert, H.; Vannahme, J.; Reiner, C.; Zaiß, T.; Schlosser, M. Li$_6$PS$_5$X: A Class of Crystalline Li-Rich Solids with an Unusually High Li$^+$ Mobility. *Angew. Chem., Int. Ed.* **2008**, *47*, 755−758.

(4) Deiseroth, H.-J.; Maier, J.; Weichert, K.; Nickel, V.; Kong, S.-T.; Reiner, C. Li$_7$PS$_6$ and Li$_6$PS$_5$X (X: Cl, Br, I): Possible Three-Dimensional Diffusion Pathways for Lithium Ions and Temperature Dependence of the Ionic Conductivity by Impedance Measurements. *Z. Anorg. Allg. Chem.* **2011**, *637*, 1287−1294.

(5) Lee, Y.-G.; Fujiki, S.; Jung, C.; Suzuki, N.; Yashiro, N.; Omoda, R.; Ko, D.-S.; Shiratsuchi, T.; Sugimoto, T.; Ryu, S.; Ku, J. H.; Watanabe, T.; Park, Y.; Aihara, Y.; Im, D.; Han, I. T. High-Energy Long-Cycling All-Solid-State Lithium Metal Batteries Enabled by Silver-Carbon Composite Anodes. *Nat. Energy* **2020**, *5*, 299−308.

(6) Wang, S.; Zhang, Y.; Zhang, X.; Liu, T.; Lin, Y.-H.; Shen, Y.; Li, L.; Nan, C.-W. High-Conductivity Argyrodite Li$_6$PS$_5$Cl Solid Electrolytes Prepared via Optimized Sintering Processes for All-Solid-State Lithium-Sulfur Batteries. *ACS Appl. Mater. Interfaces* **2018**, *10*, 42279−42285.

(7) Schwietert, T. K.; Arszelewska, V. A.; Wang, C.; Yu, C.; Vasileiadis, A.; de Klerk, N. J. J.; Hageman, J.; Hupfer, T.; Kerkamm, I.; Xu, Y.; van der Maas, E.; Kelder, E. M.; Ganapathy, S.; Wagemaker, M. Clarifying the Relationship between Redox Activity and Electrochemical Stability in Solid Electrolytes. *Nat. Mater.* **2020**, *19*, 428−435.

(8) Tan, D. H. S.; Wu, E. A.; Nguyen, H.; Chen, Z.; Marple, M. A. T.; Doux, J.-M.; Wang, X.; Yang, H.; Banerjee, A.; Meng, Y. S. Elucidating Reversible Electrochemical Redox of Li$_6$PS$_5$Cl Solid Electrolyte. *ACS Energy Lett.* **2019**, *4*, 2418−2427.

(9) Auvergniot, J.; Cassel, A.; Ledeuil, J.-B.; Viallet, V.; Seznec, V.; Dedryvère, R. Interface Stability of Argyrodite Li$_6$PS$_5$Cl toward LiCoO$_2$, LiNi$_{1/3}$Co$_{1/3}$Mn$_{1/3}$O$_2$, and LiMn$_2$O$_4$ in Bulk All-Solid-State Batteries. *Chem. Mater.* **2017**, *29*, 3883−3890.

(10) Kraft, M. A.; Culver, S. P.; Calderon, M.; Böcher, F.; Krauskopf, T.; Senyshyn, A.; Dietrich, C.; Zevalkink, A.; Janek, J.; Zeier, W. G. Influence of Lattice Polarizability on the Ionic Conductivity in the Lithium Superionic Argyrodites Li$_6$PS$_5$X (X = Cl, Br, I). *J. Am. Chem. Soc.* **2017**, *139*, 10909−10918.

(11) Rayavarapu, P. R.; Sharma, N.; Peterson, V. K.; Adams, S. Variation in Structure and Li$^+$-Ion Migration in Argyrodite-Type Li$_6$PS$_5$X (X = Cl, Br, I) Solid Electrolytes. *J. Solid State Electrochem.* **2012**, *16*, 1807−1813.

(12) Deng, Z.; Zhu, Z.; Chu, I.-H.; Ong, S. P. Data-Driven First-Principles Methods for the Study and Design of Alkali Superionic Conductors. *Chem. Mater.* **2017**, *29*, 281−288.

(13) Chen, H. M.; Maohua, C.; Adams, S. Stability and Ionic Mobility in Argyrodite-Related Lithium-Ion Solid Electrolytes. *Phys. Chem. Chem. Phys.* **2015**, *17*, 16494−16506.

(14) Zhang, Z.; Sun, Y.; Duan, X.; Peng, L.; Jia, H.; Zhang, Y.; Shan, B.; Xie, J. Design and Synthesis of Room Temperature Stable Li-Argyrodite Superionic Conductors via Cation Doping. *J. Mater. Chem. A* **2019**, *7*, 2717−2722.

(15) Huang, W.; Cheng, L.; Hori, S.; Suzuki, K.; Yonemura, M.; Hirayama, M.; Kanno, R. Ionic Conduction Mechanism of a Lithium Superionic Argyrodite in the Li-Al-Si-S-O System. *Mater. Adv.* **2020**, *1*, 334−340.

(16) Feng, X.; Chien, P.-H.; Wang, Y.; Patel, S.; Wang, P.; Liu, H.; Immediato-Scuotto, M.; Hu, Y.-Y. Enhanced Ion Conduction by Enforcing Structural Disorder in Li-Deficient Argyrodites Li$_{6-x}$PS$_{5-x}$Cl$_{1+x}$. *Energy Storage Mater.* **2020**, *30*, 67−73.

(17) Kraft, M. A.; Ohno, S.; Zinkevich, T.; Koerver, R.; Culver, S. P.; Fuchs, T.; Senyshyn, A.; Indris, S.; Morgan, B. J.; Zeier, W. G. Inducing High Ionic Conductivity in the Lithium Superionic Argyrodites Li$_{6+x}$P$_{1-x}$Ge$_x$S$_5$I for All-Solid-State Batteries. *J. Am. Chem. Soc.* **2018**, *140*, 16330−16339.

(18) Adeli, P.; Bazak, J. D.; Park, K. H.; Kochetkov, I.; Huq, A.; Goward, G. R.; Nazar, L. F. Boosting Solid-State Diffusivity and Conductivity in Lithium Superionic Argyrodites by Halide Substitution. *Angew. Chem., Int. Ed.* **2019**, *58*, 8681−8686.

(19) Wang, P.; Liu, H.; Patel, S.; Feng, X.; Chien, P.-H.; Wang, Y.; Hu, Y.-Y. Fast Ion Conduction and Its Origin in Li$_{6-x}$PS$_5$Br$_{1+x}$. *Chem. Mater.* **2020**, *32*, 3833−3840.

(20) Zhou, L.; Assoud, A.; Zhang, Q.; Wu, X.; Nazar, L. F. New Family of Argyrodite Thioantimonate Lithium Superionic Conductors. *J. Am. Chem. Soc.* **2019**, *141*, 19002−19013.

(21) Kong, S.-T.; Deiseroth, H.-J.; Reiner, C.; Gün, Ö.; Neumann, E.; Ritter, C.; Zahn, D. Lithium Argyrodites with Phosphorus and Arsenic: Order and Disorder of Lithium Atoms, Crystal Chemistry, and Phase Transitions. *Chem.—Eur. J.* **2010**, *16*, 2198−2206.

(22) de Klerk, N. J. J.; Rosłoń, I.; Wagemaker, M. Diffusion Mechanism of Li Argyrodite Solid Electrolytes for Li-Ion Batteries and Prediction of Optimized Halogen Doping: The Effect of Li Vacancies, Halogens, and Halogen Disorder. *Chem. Mater.* **2016**, *28*, 7955−7963.

(23) Huang, W.; Yoshino, K.; Hori, S.; Suzuki, K.; Yonemura, M.; Hirayama, M.; Kanno, R. Superionic Lithium Conductor with a Cubic Argyrodite-Type Structure in the Li-Al-Si-S System. *J. Solid State Chem.* **2019**, *270*, 487−492.

(24) Minafra, N.; Kraft, M. A.; Bernges, T.; Li, C.; Schlem, R.; Morgan, B. J.; Zeier, W. G. Local Charge Inhomogeneity and Lithium Distribution in the Superionic Argyrodites Li$_6$PS$_5$X (X = Cl, Br, I). *Inorg. Chem.* **2020**, *59*, 11009−11019.

(25) Masuda, N.; Kobayashi, K.; Utsuno, F.; Uchikoshi, T.; Kuwata, N. Effects of Halogen and Sulfur Mixing on Lithium-Ion Conductivity in Li$_{7-x-y}$(PS$_4$)(S$_{2-x-y}$Cl$_x$Br$_y$) Argyrodite and the Mechanism for Enhanced Lithium Conduction. *J. Phys. Chem. C* **2022**, *126*, 14067−14074.

(26) Morgan, B. Mechanistic Origin of Superionic Lithium Diffusion in Anion-Disordered Li$_6$PS$_5$X Argyrodites. *Chem. Mater.* **2021**, *33*, 2004.

(27) Hanghofer, I.; Brinek, M.; Eisbacher, S. L.; Bitschnau, B.; Volck, M.; Hennige, V.; Hanzu, I.; Rettenwander, D.; Wilkening, H. M. R. Substitutional Disorder: Structure and Ion Dynamics of the Argyrodites Li6PS5Cl, Li6PS5Br and Li6PS5I. *Phys. Chem. Chem. Phys.* **2019**, *21*, 8489−8507.

(28) Lattice Dynamics and Ionic Motion in Super Ionic in Conductors. In *Superionic Conductors*; Mahan, G. D., Roth, W. L., Eds.; Springer US: Boston, MA, 1976; p 201.

(29) Boyce, J. B.; Hayes, T. M. Structural Studies of Superionic Conduction. In *EXAFS Spectroscopy: Techniques and Applications*; Teo, B. K., Joy, D. C., Eds.; Springer US: Boston, MA, 1981; pp 103−125.

(30) Wakamura, K. Roles of Phonon Amplitude and Low-Energy Optical Phonons on Superionic Conduction. *Phys. Rev. B: Condens. Matter Mater. Phys.* **1997**, *56*, 11593−11599.

(31) Muy, S.; Bachman, J. C.; Giordano, L.; Chang, H.-H.; Abernathy, D. L.; Bansal, D.; Delaire, O.; Hori, S.; Kanno, R.; Maglia, F.; Lupart, S.; Lamp, P.; Shao-Horn, Y. Tuning Mobility and Stability of Lithium Ion Conductors Based on Lattice Dynamics. *Energy Environ. Sci.* **2018**, *11*, 850−859.

(32) Jansen, M. Volume Effect or Paddle-Wheel Mechanism—Fast Alkali-Metal Ionic Conduction in Solids with Rotationally Disordered Complex Anions. *Angew. Chem., Int. Ed.* **1991**, *30*, 1547−1558.

(33) Hanghofer, I.; Gadermaier, B.; Wilkening, H. M. R. Fast Rotational Dynamics in Argyrodite-Type Li_6PS_5X (X: Cl, Br, I) as Seen by ^{31}P Nuclear Magnetic Relaxation-On Cation-Anion Coupled Transport in Thiophosphates. *Chem. Mater.* **2019**, *31*, 4591−4597.

(34) Brinek, M.; Hiebl, C.; Hogrefe, K.; Hanghofer, I.; Wilkening, H. M. R. Structural Disorder in Li_6PS_5I Speeds ^7Li Nuclear Spin Recovery and Slows Down ^{31}P Relaxation-Implications for Translational and Rotational Jumps as Seen by Nuclear Magnetic Resonance. *J. Phys. Chem. C* **2020**, *124*, 22934.

(35) Argyrodit, W. A.; Silbererz, E. N. *Neues Jahrbuch für Mineralogie, Geognosie, Geologie und Petrefaktenkunde*; Schweizerbart, 1886; Vol. *2*, pp 67−71.

(36) Geller, S. The Crystal Structure of Gamma-Ag_8GeTe_6, a Potential Mixed Electronic-Ionic Conductor. *Z. Kristallogr.* **1979**, *149*, 31.

(37) Kato, Y.; Hori, S.; Saito, T.; Suzuki, K.; Hirayama, M.; Mitsui, A.; Yonemura, M.; Iba, H.; Kanno, R. High-Power All-Solid-State Batteries Using Sulfide Superionic Conductors. *Nat. Energy* **2016**, *1*, 16030.

(38) Hanghofer, I.; Redhammer, G. J.; Rohde, S.; Hanzu, I.; Senyshyn, A.; Wilkening, H. M. R.; Rettenwander, D. Untangling the Structure and Dynamics of Lithium-Rich Anti-Perovskites Envisaged as Solid Electrolytes for Batteries. *Chem. Mater.* **2018**, *30*, 8134−8144.

(39) Wang, F.; Evans, H. A.; Kim, K.; Yin, L.; Li, Y.; Tsai, P.-C.; Liu, J.; Lapidus, S. H.; Brown, C. M.; Siegel, D. J.; Chiang, Y.-M. Dynamics of Hydroxyl Anions Promotes Lithium Ion Conduction in Antiperovskite Li_2OHCl. *Chem. Mater.* **2020**, *32*, 8481−8491.

(40) Sears, V. F. Neutron Scattering Lengths and Cross Sections. *Neutron News* **1992**, *3* (3), 26−37.

(41) Momma, K.; Ikeda, T.; Belik, A. A.; Izumi, F. Dysnomia, a Computer Program for Maximum-Entropy Method (MEM) Analysis and Its Performance in the MEM-Based Pattern Fitting. *Powder Diffr.* **2013**, *28*, 184−193.

(42) Chen, H.; Adams, S. Bond Softness Sensitive Bond-Valence Parameters for Crystal Structure Plausibility Tests. *IUCrJ* **2017**, *4*, 614−625.

(43) Chen, H.; Wong, L. L.; Adams, S. SoftBV - a Software Tool for Screening the Materials Genome of Inorganic Fast Ion Conductors. *Acta Crystallogr., Sect. B: Struct. Sci., Cryst. Eng. Mater.* **2019**, *75* (1), 18−33.

(44) Zhang, Z.; Zou, Z.; Kaup, K.; Xiao, R.; Shi, S.; Avdeev, M.; Hu, Y.; Wang, D.; He, B.; Li, H.; Huang, X.; Nazar, L. F.; Chen, L. Correlated Migration Invokes Higher Na^+-Ion Conductivity in NaSICON-Type Solid Electrolytes. *Adv. Energy Mater.* **2019**, *9*, 1902373.

(45) Asano, T.; Sakai, A.; Ouchi, S.; Sakaida, M.; Miyazaki, A.; Hasegawa, S. Solid Halide Electrolytes with High Lithium-Ion Conductivity for Application in 4 V Class Bulk-Type All-Solid-State Batteries. *Adv. Mater.* **2018**, *30*, 1803075.

(46) Adams, S.; Rao, R. P. Understanding Ionic Conduction and Energy Storage Materials with Bond-Valence-Based Methods. In *Bond Valences*; Brown, I. D., Poeppelmeier, K. R., Eds.; Structure and Bonding; Springer, 2014; Vol. *158*, pp 129−160.

(47) Evain, M.; Gaudin, E.; Boucher, F.; Petricek, V.; Taulelle, F. Structures and Phase Transitions of the A_7PSe_6 (A = Ag, Cu) Argyrodite-Type Ionic Conductors. I. Ag_7PSe_6. *Acta Crystallogr., Sect. B: Struct. Sci.* **1998**, *54*, 376−383.

(48) Gaudin, E.; Boucher, F.; Petricek, V.; Taulelle, F.; Evain, M. Structures and Phase Transitions of the A_7PSe_6 (A = Ag, Cu) Argyrodite-Type Ionic Conductors. II. b- and c-Cu_7PSe_6. *Acta Crystallogr., Sect. B: Struct. Sci.* **2000**, *56*, 402−408.

(49) Ouyang, B.; Wang, Y.; Sun, Y.; Ceder, G. Computational Investigation of Halogen-Substituted Na Argyrodites as Solid-State Superionic Conductors. *Chem. Mater.* **2020**, *32*, 1896−1903.

(50) Patel, S. V.; Banerjee, S.; Liu, H.; Wang, P.; Chien, P.-H.; Feng, X.; Liu, J.; Ong, S. P.; Hu, Y.-Y. Tunable Lithium-Ion Transport in Mixed-Halide Argyrodites $Li_{6-x}PS_5ClBr_x$: An Unusual Compositional Space. *Chem. Mater.* **2021**, *33*, 1435−1443.

(51) Gorai, P.; Famprikis, T.; Singh, B.; Stevanović, V.; Canepa, P. Devil is in the Defects: Electronic Conductivity in Solid Electrolytes. *Chem. Mater.* **2021**, *33*, 7484−7498.

(52) Coelho, A. A. TOPAS and TOPAS-Academic : An Optimization Program Integrating Computer Algebra and Crystallographic Objects Written in C++. *J. Appl. Crystallogr.* **2018**, *51*, 210−218.

(53) Lobanov, N. N.; Alte da Veiga, L. *6th European Powder Diffraction Conference*, Abstract P12-16, Aug. 22−25, 1998.

(54) Momma, K.; Ikeda, T.; Belik, A. A.; Izumi, F. Dysnomia, a Computer Program for Maximum-Entropy Method (MEM) Analysis and Its Performance in the MEM-Based Pattern Fitting. *Powder Diffr.* **2013**, *28*, 184−193.

(55) Petříček, V.; Dušek, M.; Palatinus, L. Crystallographic Computing System JANA2006: General Features. *Z. Kristallogr.-Cryst. Mater.* **2014**, *229*, 345−352.

(56) Momma, K.; Izumi, F. VESTA : A Three-Dimensional Visualization System for Electronic and Structural Analysis. *J. Appl. Crystallogr.* **2008**, *41*, 653−658.

(57) Kresse, G.; Furthmüller, J. Efficient iterative schemes forab initiototal-energy calculations using a plane-wave basis set. *Phys. Rev. B: Condens. Matter Mater. Phys.* **1996**, *54*, 11169−11186.

(58) Perdew, J. P.; Burke, K.; Ernzerhof, M. Generalized Gradient Approximation Made Simple. *Phys. Rev. Lett.* **1996**, *77*, 3865−3868.

(59) Nosé, S. A unified formulation of the constant temperature molecular dynamics methods. *J. Chem. Phys.* **1984**, *81*, 511−519.